ACS OMEGA

http://pubs.acs.org/journal/acsodf

Article

Insight into the Adsorption and Photocatalytic Behaviors of an Organo-bentonite/Co_3O_4 Green Nanocomposite for Malachite Green Synthetic Dye and Cr(VI) Metal Ions: Application and Mechanisms

Mohamed Abdel Salam, Mostafa R. Abukhadra,* and Alyaa Adlii

Cite This: *ACS Omega* 2020, 5, 2766−2778

Read Online

ACCESS | Metrics & More | Article Recommendations | Supporting Information

ABSTRACT: A green composite of organically modified bentonite supported by Co_3O_4 nanoparticles (OB/Co) was successfully fabricated and investigated as a potential eco-friendly, low-cost adsorbent and photocatalyst for promising removal of both malachite green dye (MG.D) and Cr(VI) ions. The composite showed high adsorption properties and achieved experimental q_{max} values of 223 and 139 mg/g for MG.D and Cr(VI) after equilibration times of 360 min and 480 min for the inspected contaminants, respectively. The kinetic and equilibrium inspection reflected the best description of their adsorption behaviors by the pseudo-first-order kinetic model and the Langmuir isotherm model, respectively. This revealed favorable and homogeneous uptake of both MG.D and Cr(VI) in a monolayer form with theoretical Langmuir q_{max} values of 343.6 and 194.5 mg/g, respectively. The theoretical adsorption energies of MG.D (0.6 kJ/mol) and Cr(VI) (0.5 kJ/mol) from the Dubinin−Radushkevich (D−R) model revealed physisorption properties that might be resulted from some types of Coulombic attractive forces, achieving theoretical q_{max} values of 226.5 and 144.6 mg/g, respectively. The suggested adsorption mechanism was confirmed by the main mathematical parameters of thermodynamic studies that revealed physical, spontaneous, and exothermic uptake processes. Also, the composite showed high photocatalytic performance under visible light, which resulted in a 100% removal percentage of 100 mg/L of MG.D and Cr(VI) after about 180 and 240 min, respectively, from the adsorption equilibrium time.

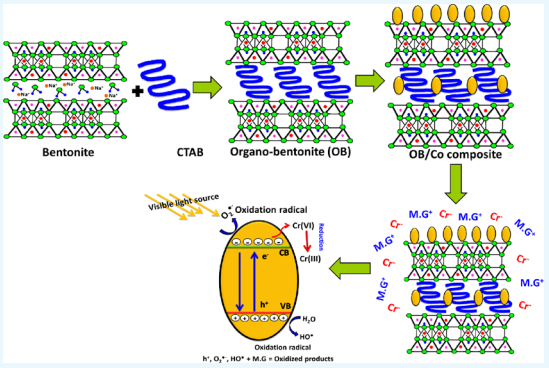

1. INTRODUCTION

Decontamination of both organic and inorganic water pollutants using natural adsorbents and photocatalysts was endorsed widely as an effective, cheap, and simple technique.[1−3] Among the commonly detected hazardous organic pollutants, malachite green synthetic dye (MG.D) was characterized as one of the highly toxic synthetic dyes that are used extensively in several applications including aquaculture, food, and medical disinfectants.[4,5] Carcinogenesis, mutagenesis, chromosomal fractures, respiratory toxicity, and teratogenicity are common diseases recorded for MG.D contaminants.[2] Hexavalent chromium (Cr(VI)) is one of the reported carcinogenic inorganic water contaminants, and its safety limit in drinking water is set to be 5 μg/L.[6,7]

The previous toxic impacts attracted the attention of scientific, health, and environmental authorities to develop promising techniques to reduce the concentrations of such pollutants in water resources.[1] Therefore, great efforts have been made by the interested researchers to develop advanced materials as single phases or composites that can be produced by simple methods at low costs and exhibit high adsorption and photocatalytic activity.[2,8−10] Transitional metal oxides and hybrid composites based on them were addressed extensively as adsorbents and heterogeneous photocatalysts.[11−13] The green fabrication of metal oxide nanoparticles utilizing the green extracts of plants and vegetables was recommended strongly to produce environmental materials for remediation applications.[14,15] The green fabricated metal oxides have considerably low cost, nontoxicity, biodegradability, promising surface area, significant surface reactivity, and high selectivity properties. Moreover, the commonly used green extracts exhibit strong reducing effects and act as coating agents, which minimizes the expected agglomeration of the target metal oxides during the synthesis processes.[14,15]

Generally, supporting the metal oxides either by the usual chemical process or the green methods into suitable carriers enhances the surface area, adsorption capacity, and recovery properties of such nanoparticles.[6,16] Natural layered materials of bentonite, montmorillonite, and kaolinite were studied as promising catalyst carriers of high physicochemical features,

Received: October 14, 2019
Accepted: January 23, 2020
Published: February 4, 2020

https://dx.doi.org/10.1021/acsomega.9b03411
ACS Omega 2020, 5, 2766−2778

high natural availability, and low cost.[2,17] Bentonite was studied as one of the best natural catalyst carriers for its low cost, flexible chemical and crystalline structure, high ion exchange, promising adsorption properties, and high safety properties.[18] It was applied already as a carrier for several types of photocatalysts including nano-ZnO, Cu_2O, CdS, Ru-TiO_2, Ag_3PO_4, TiO_2, Ni_2O_3, and Bi_2O_3.[1,19−23] Unfortunately, most of the performed studies focused on using bentonite as a carrier in its pure phase without further modifications, which is of lower surface area and adsorption capacity than its modified products.[24]

The modification of bentonite by the different chemical and physical processes including alkaline treatment, acid leaching, thermal treatment, polymer intercalation, and organic modifications resulted in hybrid materials of high basal spacing, high surface area, and high adsorption capacities and having more active functional groups and high affinity for organic pollutants.[25] Therefore, the introduction of organo-bentonite (OB) as a carrier for cobalt oxide nanoparticles can give promising adsorption and photocatalytic results as compared to the regular use of bentonite or other clay minerals in their pure phases. The organic modification gives the bentonite higher surface area and higher adsorption capacity than those of the raw phase especially for the organic pollutants, which is considered as a vital stage for effective photocatalytic degradation and reduction processes.[26,27] Additionally, the synthesis of cobalt oxide by the green method can give the composite some technical and environmental values as it becomes eco-friendly and its particles can be formed with minimum agglomeration probabilities.

Therefore, the aim of the study is to address, for the first time, the application of organically modified bentonite as a carrier for green fabricated cobalt oxide nanoparticles as a novel green nanocomposite (organo-bentonite/Co_3O_4, OB/Co) with enhanced adsorption and photocatalytic performances for organic malachite green synthetic dye (MG.D) and inorganic Cr(VI) metal. The adsorption behaviors and performances were evaluated considering the main affecting parameters and the controlling mechanisms and taking into account the theoretical assumptions of the common kinetic and equilibrium models. Moreover, the photocatalytic properties of organo-bentonite/Co_3O_4 in the oxidation of MG.D and the reduction of Cr(VI) metals into Cr(III) ions were studied with a declaration of the main mechanism.

2. RESULTS AND DISCUSSION

2.1. Characterization. *2.1.1. Structural and Crystalline Properties.* The structural features of bentonite, OB, and OB/Co composite were examined considering their X-ray diffraction (XRD) patterns (Figure 1). The inspected pattern of the used raw bentonite showed the dominance of montmorillonite mineral as the principal phase (Figure 1A). Kaolinite mineral was distinguished as nonswelling clay impurities in the sample in addition to calcite and quartz minerals as nonclay impurities. The present montmorillonite was characterized by its demonstrative XRD peak at about 5.78°, which is the corresponding peak of the (001) plane in its orthorhombic crystal (ref card No. 000-003-0010 and No. 00-058-201). Also, other descriptive peaks were identified at about 6.95, 19.85, 21.54, 26.68, and 28.56° as insignificant peaks (Figure 1A). Regarding the crystallinity of montmorillonite, it was formed with 12.71 Å as the basal spacing and 12.96 nm as the average crystallite size.

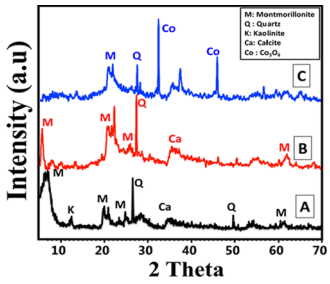

Figure 1. XRD patterns of raw bentonite (A), organic modified bentonite (OB) (B), and organo-bentonite/Co_3O_4 composite (OB/Co) (C).

The synthesis of organo-bentonite by direct intercalation of its layer by cetyltrimethylammonium bromide (CTAB) (OB) was confirmed by the XRD analysis (Figure 1B). It displays the reported peaks for the raw bentonite with noticeable deviation for them from their positions without any detection of new peaks. The principal peaks were detected at 4.52 and 6.79° instead of at 5.78 and 6.95°, which were identified in the raw bentonite sample with a significant increase in its basal spacing to be 19.52 Å, confirming the successful intercalation process of montmorillonite layers by the CTAB chains (Figure 1B). The reported augmentation in the basal spacing of OB is related to the expected orientation of the organic chains of CTAB within the montmorillonite sheets.

After the support of OB by green cobalt oxide particles, the XRD pattern showed two characteristic peaks of cobalt oxide as a Co_3O_4 phase at about 31.74 and 45.49°, which are the two theta angles of the (111) and (200) crystallographic planes (JCPDS No. 42-1467) (Figure 1C). The montmorillonite peaks appeared highly reduced in the composite, especially the main peaks that disappeared completely in the sample, which can give strong indications about the precipitation of cobalt oxide particles on the surface of OB.

2.1.2. Morphological Properties. The surficial morphological features in addition to the internal structures of bentonite, OB, and OB/Co composite were studied considering the captured scanning electron microscopy (SEM) images and high-resolution transmission electron microscopy (HRTEM) images, respectively (Figure 2). The used bentonite sample appeared as well-developed montmorillonite platelets, which were partially ornamented by minute particles related to the existing nonclay impurities (Figure 2A). The observed montmorillonite platelets showed flexed forms and displayed the common edge-to-face structural mode (EF mode), forming a secondary porous matrix of lenticular shape. Such morphological phenomenon is attributed to the predicted random agglomeration of the present montmorillonite sheets.[19] The HRTEM images showed the characteristic multilayered structure of bentonite with clear detection of the distinctive lattice fingers (Figure 2B,C).

The integration between CTAB and bentonite in OB reflected a noticeable expansion between the bentonite layers and obvious changes in the external morphology as it appeared as partially rounded particles of irregular topography (Figure 2D). This was supported by the TEM image, as the organo-bentonite grains were distinguished as nearly spherical layers arranged regularly above each other (Figure 2E). The green support of OB by Co_3O_4 was also confirmed by the SEM and TEM images. The SEM images revealed the presence of cobalt oxide as fine particles of elliptical to spherical shapes and were

https://dx.doi.org/10.1021/acsomega.9b03411
ACS Omega 2020, 5, 2766−2778

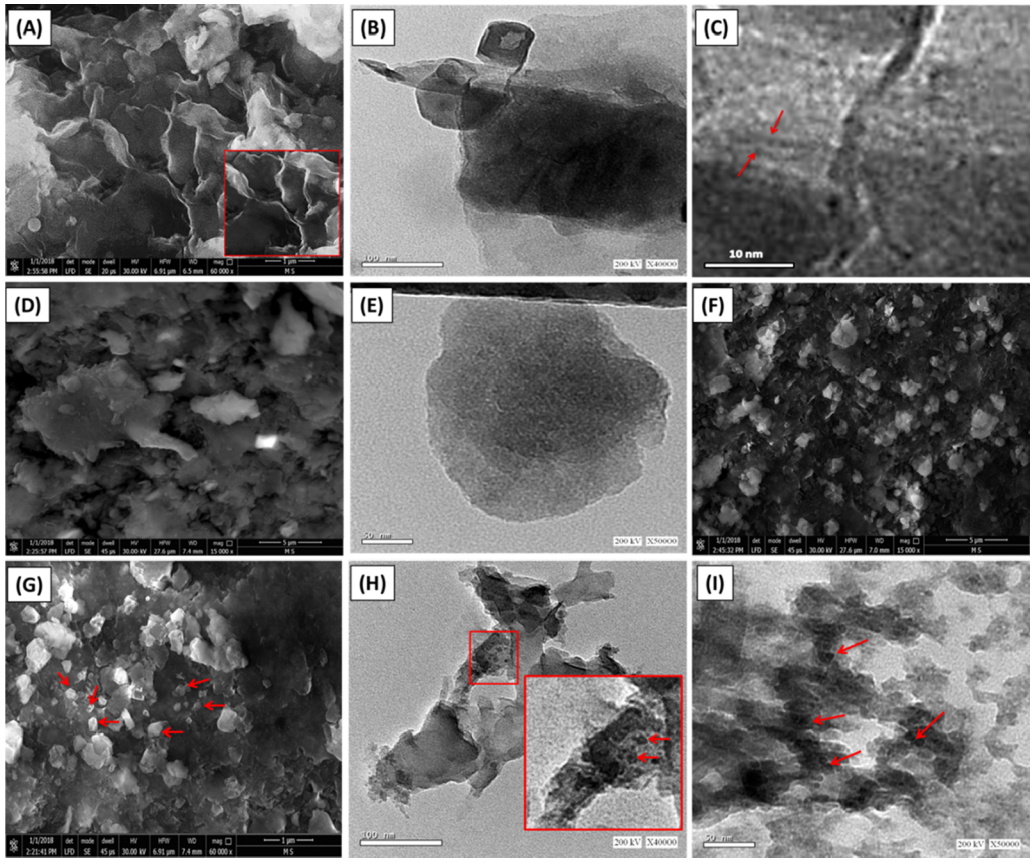

Figure 2. (A) SEM morphology of bentonite, (B and C) TEM images of bentonite, (D) SEM image of organically modified bentonite (OB), (E) TEM image of organically modified bentonite, (F) and (G) SEM images of organo-bentonite supported by green Co_3O_4 (OB/Co), and (H) and (I) TEM images of organo-bentonite supported by green Co_3O_4 (OB/Co).

Table 1. FT-IR Spectral Bands of Bentonite, CTAB, OB, and OB/Co and Their Related Groups

positions (cm^{-1})				
BE	CTAB	OB	OB/Co	chemical functional groups
3480		3478.4	3475.6	structural OH group and adsorbed water[2]
	3017.6			N−H stretching[28,29]
	2918.2	2914	2914.3	asymmetrical C−H stretching[30,31]
	2849.2	2825	2836.2	symmetrical C−H stretching[28,31]
1640.6		1654	1648	water within the interlayers[18]
	1486.8	1495	1485.7	C−N stretching[28]
	1473.4			excited methylene group[28]
	1463.1			C−N stretching[28]
	1056.3			C−N stretching[29]
1000		1084	1065	Si−O group[17]
918				Al−O groups[1]
	719−730			C−C stretching vibration[28]
			570 and 668	the vibration stretching of the O−Co bonds in Co_3O_4[32]
400−1000		400−1000	400−1000	Si−O−Al, Mg−Fe−OH, and Si−O−Mg[1]

distributed randomly on the surface of OB as decorated grains (Figure 2F,G). The TEM images showed the presence of Co_3O_4 as random nanoparticles of spherical shape and disseminated on the surface of organo-bentonite particles (Figure 2H,I). Such morphological properties can give the final product a high surface area, and the distribution of cobalt oxide on the surface of OB without agglomeration will provide high exposed properties for it as an active photocatalyst to be of high interaction properties with the incident light photons.

The successful integration between bentonite, CTAB, and Co_3O_4 in a composite (OB/Co) resulted in a considerable enhancement in the textural properties as compared to the individual components. The measured surface area increased by 91, 94.8, and 104.6 m^2/g for bentonite, OB, and OB/Co, respectively, which can be related to the expansion of bentonite layers by the CTAB organic surfactant and surficial distribution of Co_3O_4 as nano-nudes.

2.1.3. Chemical Functional Groups. The energy-dispersive X-ray spectroscopy (EDX) analysis confirmed the presence of

https://dx.doi.org/10.1021/acsomega.9b03411
ACS Omega 2020, 5, 2766−2778

Al, Si, O, C, and Co as the main components of the composite (Figure S1). The functional groups of the composite in comparison with the individual components confirm the successful combination of bentonite, CTAB, and Co_3O_4 (Figure S2 Supporting Information). The Fourier-transform infrared (FT-IR) spectral bands of bentonite, CTAB, OB, and the OB/Co composite are shown in Figure S2, and the characteristic chemical groups are listed in Table 1. The bentonite precursor displayed distinctive absorption bands related to Si−O−Si groups, OH groups, and Al−O groups, which signify the structure of clay minerals (Table 1). Also, the used organic surfactant exhibited the representative bands of cetyltrimethylammonium bromide related to C−H groups, C−N groups, and C−C groups (Figure S2 and Table 1). The successful intercalation of the addressed bentonite layers with CTAB chains in organo-bentonite (OB) resulted in an FT-IR spectrum containing complex bands related to both the functional groups of bentonite and the functional groups of CTAB (Figure S2 and Table 1). Additionally, there is an obvious fluctuation in the reported original positions of the main bands of bentonite and CTAB, which gives a strong indication about the interaction between bentonite and TAB (Figure S2). Such deviation was also observed after the support of OB by Co_3O_4 in addition to the observable identification of the O−Co bond of Co_3O_4 (Table 1 and Figure S2).

2.2. Adsorption Results. *2.2.1. Effect of the Main Parameters. 2.2.1.1. Effect of pH.* Adjusting the pH value is of vital importance in any studied organic or inorganic adsorption system as it controls the surface charges of the adsorbents and the state of the studied dissolved ions as well as the predicted competition between H^+ and OH^- on the uptake sites.[33] Regarding the speciation of Cr(VI), it exists in three anionic forms including $Cr_2O_7^{2-}$, $HCrO^{4-}$, and CrO_4^{2-} with dominance for $Cr_2O_7^{2-}$ and $HCrO^{4-}$ in the range from about pH 2 to about pH 6 and is present as chromate anions at pH values higher than pH 6.[2,6]

As for the results obtained for the removal of MG.D, there is a noticeable increment in the achieved removal percentages from about 24.2% to about 68% with a consistent increase in the adjusted pH of the solutions from 3 to about 8 (Figure 3A). The adverse behavior was recognized for the Cr(VI) metal as the removal percentages reflected a continuous reduction in the values with the systematic augmentation in the pH value in the same manner from 62.3% (pH 3) to 26.7% (pH 8) (Figure 3A). The recorded behaviors are in good agreement with other studies introduced for MG.D as well as the Cr(VI) metal.[2,18] The predicted protonation of the OB/Co surface with a change of the nature of the medium from acidic to alkaline and the associated saturation of it by negative charges make the composite exhibit high attractive properties for positive ions (MG dye) and high repulsion properties for negative ions (Cr(VI)).[33] Such explanation was supported by the measured pH (PZC) of OB/Co, which is 6.32, and this reflected the dominance of the positive charges at pH values lower than 6.32 and the negative charges at pH values higher than 6.32.

2.2.1.2. Effect of Time. Detection of the equilibrium uptake time as the best time for the investigated adsorbents is of critical commercial value. For MG.D as well as the Cr(VI) metal, the curves displayed two different adsorption stages of different uptake rates (Figure 3B). This appeared in the rapid changes of the adsorbed quantity with the systematic expansion in the interaction time, representing the first stage

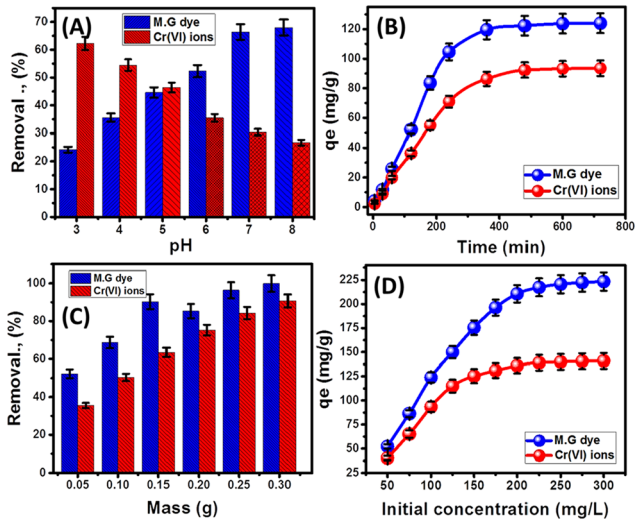

Figure 3. Effect of the experimental parameters on the adsorption of the MG dye and Cr(VI) metals: (A) solution pH, (B) contact time, (C) OB/Co masses, and (D) initial concentrations of the examined pollutants.

(Figure 3B). This stage was followed by another stage, which appeared as a plateau curve with slight changes in MG.D and Cr(VI) metal adsorbed quantities, reflecting the realization of their equilibrium states (Figure 3B). Such trends were reported in the literature and explained by the continuous occupation of OB/Co-active sites by MG.D molecules and the Cr(VI) metal until the whole occupation of the existing sites.[34,35] The experimental equilibrium intervals for MG.D and Cr(VI) metal were accomplished after 360 min and 480 min, respectively, realizing uptake capacities of 124 and 93.5 mg/g, respectively (Figure 3B).

2.2.1.3. Adsorbent Dosage. The possible augmentation in the decontamination of MG.D and Cr metals considering the increase in the OB/Co masses was addressed and is displayed in Figure 3C. From the figure, it was observed that the decontamination percentages of MG.D were expanded by 52.3, 68.7, 90.3, 85.3, 96.4, and 99.4% on increasing the incorporated OB/Co masses by 0.05, 0.1, 0.15, 0.2, 0.25, and 0.3 g, respectively (Figure 3C). As for Cr(VI) ions, their decontamination by the OB/Co composite showed a significant increase by 35.5, 50.4, 63.5, 75.2, 84.4, and 90.7% with a systematic increment in OB/Co masses from the previous values (Figure 3C). The noticeable improvement in the decontamination percentages with the higher masses of the composite was associated with the predicted increase in the exposed surface area of OB/Co as well as the reacting active sites.[36]

2.2.1.4. Initial Concentrations. The systematic evaluation of the adsorption capacity of OB/Co for MG.D and Cr metals using different concentrations plays a principal role in detecting the experimental maximum saturation capacity and gives an effective contribution in understanding the controlling mechanism. This was accomplished considering the studied concentration from 50 mg/L to about 300 mg/L, and the results are emphasized graphically in Figure 3D. The two curves reflected the ability of OB/Co to adsorb more of MG.D molecules and Cr(VI) metal with persistent increment in the used concentrations until the full occupation of the receptor sites at a certain concentration, representing the equilibrium concentration (Figure 3D). The experiment equilibrium for

https://dx.doi.org/10.1021/acsomega.9b03411
ACS Omega 2020, 5, 2766−2778

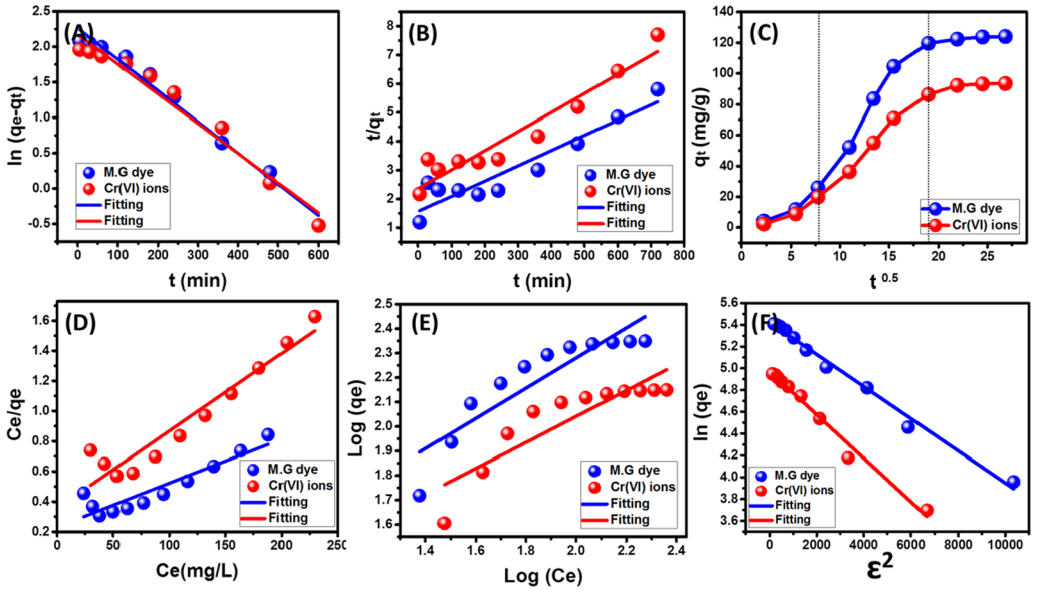

Figure 4. Linear fitting with the pseudo-first-order model (A), the pseudo-second-order model (B), the intraparticle diffusion model (C), the Langmuir model (D), the Freundlich isotherm model (E), and the Dubinin−Radushkevich isotherm model (F).

MG.D was reached after using a concentration of 250 mg/L, achieving 223 mg/g as the maximum experimental adsorption capacity (Figure 3D). For Cr(VI), the equilibration concentration was 225 mg/L and 139 mg/g was realized as the maximum capacity. Moreover, the MG.D and Cr(VI) curves are L-type (2 L) isotherm curves that are associated with adsorbents of very high affinity to the target pollutants.[37,38]

2.2.2. Kinetics and Equilibrium Properties. 2.2.2.1. Kinetic Behavior. Regarding the kinetic behavior of the OB/Co system, the linear fitting of the uptake results of MG.D and Cr(VI) metal with the four reported theoretical models is emphasized in Figure 4A−C. The fitting results and the calculated theoretical mathematical parameters revealed excellent agreement with the hypothesis of the pseudo-first-order kinetic model and pseudo-second-order model, achieving a high correlation coefficient close to unity either for MG.D or for the Cr(VI) metal with obvious preference for the pseudo-first-order model (Table 2). Such fitting results suggested a dominant physisorption mechanism associated with the influence of some chemical effects that can include complexion or ion exchange processes.[2,39] The good fitness with the Elovich model for the two pollutants supported the previously suggested explanation of the adsorption behaviors and also reflected the energetic heterogeneous nature of OB/Co during the adsorption reactions[8] (Figure S3 and Table 2).

For the inspection of the intraparticle diffusion assumption, the curves plotted for MG.D and Cr(VI) metal demonstrated several adsorption divisions without passing by the original points, i.e., there is more than one mechanism controlling the uptake by OB/Co rather than the possible diffusion of the studied ions[6] (Figure 4C). The curves displayed three segments: The first one can be assigned to the external adsorption by the surficial receptor sites of OB/Co composites. The second segment is related to the layer adsorption stage that has limited intraparticle diffusion rate. After the formation of thick adsorbed MG.D and Cr(VI) layers on OB/Co by molecular association and interionic attraction mechanisms, the diffusion rate decreases gradually, forming the third adsorption segment that reflects the saturation or equilibration stage.[40]

Table 2. Parameters of the Examined Kinetic Models, Isotherm Models, and the Thermodynamic Studies

model name	parameters	MG.D	Cr(VI)
	Kinetic Models		
pseudo-first-order	K_1 (mg/min)	0.0044	0.0042
	q_e (Cal) (mg/g)	9.62	8.79
	R^2	0.98	0.96
pseudo-second-order	K_2 (mg/min)	1.79×10^{-5}	1.86×10^{-5}
	q_e (Cal) (mg/g)	189	151
	R^2	0.90	0.92
Elovich	β (g/mg)	0.0336	0.045
	α (mg/(g min))	316.9	253.87
	R^2	0.88	0.87
	Isotherm Models		
Langmuir	$q_{max\ (mg/g)}$	343.6	194.5
	b (L/mg)	0.0126	0.0145
	R^2	0.91	0.92
	R_L	0.21−0.61	0.19−0.58
Freundlich	$1/n$	0.61	0.53
	k_F	11.14	9.61
	R^2	0.81	0.77
Dubinin−Radushkevich	β (mol^2/KJ^2)	1.47	1.99
	q_m (mg/g)	226.5	144.6
	R^2	0.99	0.98
	E (kJ/mol)	0.6	0.5
	Thermodynamic Parameters		
$\Delta G°$ (kJ/mol)	298 K	−3.36	−1.96
	303 K	−2.98	−1.42
	308 K	−2.6	−1.19
	313 K	−2.17	−0.88
	318 K	−1.76	−0.66
	323 K	−1.52	−0.512
	328 K	−1.31	−0.356
	333 K	−1.12	−0.254
$\Delta H°$ (kJ/mol)		−23.1	−15.8
$\Delta S°$ (J/(K mol))		66.52	47.2

https://dx.doi.org/10.1021/acsomega.9b03411
ACS Omega 2020, 5, 2766−2778

2.2.2.2. Equilibrium Behavior. The equilibrium behavior for OB/Co adsorption systems was followed considering the assumptions of Langmuir (Figure 4D), Freundlich (Figure 4E), and Dubinin−Radushkevich isotherm models (Figure 4F). The Langmuir model is a commonly addressed model to designate uptake processes of the monolayer form that occur homogeneously by the reacting sites of the surface of the adsorbent.[41] On the other hand, the Freundlich model can be applied to signify the adsorption mechanisms of the multilayer form and heterogeneous type.[35,42] The linearly mathematical fitting showed excellent correlation coefficient values with the Langmuir model rather than the Freundlich model, suggesting the homogenous uptake of MG.D and Cr metal by OB/Co in the monolayer form (Table 2). Their R_L parameters revealed favorable uptake by the composite and the regular increase in their calculated values with the investigated concentrations related to the high experimental uptake capacities at the higher concentrations[43] (Table 2). Also, based on the theoretical Langmuir-related parameters, the OB/Co composite can achieve 343.6 and 194.5 mg/g as theoretical maximum capacities for MG.D and Cr metal, respectively (Table 2).

Moreover, the Dubinin−Radushkevich (D−R) model was studied to predict the principal operating mechanisms (physical or chemical) during the uptake of MG.D and Cr metal by the OB/Co composite considering the Gaussian energy distribution.[44] The accomplished results of MG.D and Cr metal are in excellent agreement with the D−R model, and its related parameters displayed 226.5 and 144.6 mg/g as the theoretical uptake capacities of MG.D and Cr metal, respectively (Table 2). The calculated adsorption energies of MG.D and Cr metal are 0.6 and 0.5 kJ/mol, respectively, which imply physisorption properties of OB/Co for MG.D and Cr metal (Table 2). The obtained results from the D−R model and the kinetic model suggested ion exchange processes that might involve weak electrostatic attraction (Coulombic attractive forces) without destruction and/or formation of chemical bonds.[41] As the adsorption results are in better agreement with the D−R model as compared to the Langmuir model, the theoretical q_{max} values obtained by the D−R model are the most appropriate values.

2.2.3. Thermodynamic Properties. The thermodynamic properties of the OB/Co adsorption system for MG.D and Cr metal were inspected considering different values for the reaction temperature. The results emphasized detectable declination in their removal capacities with a regular increase in the adsorption temperature from 298 K (132 mg/g (MG.D) and 105 mg/g (Cr metal)) to 333 K (85.6 mg/g (MG.D) and 70.8 mg/g (Cr metal)), revealing their exothermic adsorption by OB/Co[2] (Figure 5A). The Gibbs free energy values (ΔG°) at the different studied adsorption temperatures were calculated using eq 1 and are listed in Table 2[40]

$$\Delta G^\circ = -RT \ln K_c \quad (1)$$

All of the theoretical estimated ΔG° values are lower than 20 kJ/mol and of negative signs, which is a strong indication of their physisorption with spontaneous and favorable properties[35,45] (Table 2). The reported increment in the ΔG° values with the organized increase in temperature reflected linear declination in the favorable properties of the reaction the controlled expanding in the temperature.[45]

The enthalpy (ΔH°) and the entropy (ΔS°) were calculated from the linear fitting of the accomplished results with the Van't Hoff equation (eq 2; Figure 5B, Table 2).[46]

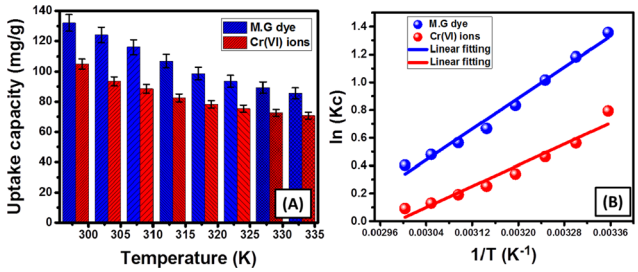

Figure 5. Uptake capacities of OB/Co for MG.D and Cr metal at different operating temperatures (A) and Van't Hoff plot for the uptake results (B).

$$\ln(K_c) = \frac{\Delta S^\circ}{R} - \frac{\Delta H^\circ}{RT} \quad (2)$$

The obtained enthalpies of MG.D and Cr metal are of negative signs, which are related to the exothermic reactions and their values established the physisorption mechanisms for the studied contaminants[2,47] (Table 2). Additionally, the positive signs that were observed for the entropy (ΔS°) signified the high affinity of OB/Co for them and suggested a significant increase in randomness possibilities during the uptake reactions[48] (Table 2).

2.2.4. Comparison Study. To investigate the uptake properties of synthetic OB/Co as compared to the commonly studied adsorbents, its theoretical and experimental maximum capacities were compared with the reported values for other adsorbents in the published literature (Table 3). The presented results reflected the preferences for using OB/Co as an adsorbent, which is represented by its high uptake capacities for MG.D and Cr metal as compared to most of the presented natural and synthetic adsorbents involving pure bentonite, diatomite, clay minerals, organoclays, some metal oxides in pure phases or as composites, some polymers, carbon nanotubes, and graphene oxide. Therefore, the synthetic OB/Co composite can be introduced as a green, low-cost, and eco-friendly adsorbent of high adsorption affinities for both synthetic organic dyes and heavy metals.

2.3. Photocatalytic Properties. The photocatalytic behavior of the OB/Co composite was studied for the oxidation and photoreduction of 100 mg/L MG.D and Cr(VI) metals, respectively (Figure 6). These were accomplished after the adsorption/desorption of the composite for both of the studied contaminants and continued for 240 min under visible light. The results reflected that the maximum removal percentages of MG.D and Cr metal by OB/Co after the equilibration were about 62 and 47%, respectively (Figure 6). Under visible light illumination, the catalytic activity of OB/Co as a potential photocatalyst resulted in systematic removal of MG.D as oxidized products by 68.5, 80, 91.4, 96.3, 98.5, and 100% after time intervals of 30, 60, 90, 120, 150, and 180 min, respectively, i.e., the complete removal of MG.D (100 mg/L) can be accomplished after 180 min of photocatalytic degradation considering the adsorption equilibrium as the start point (Figure 6).

Regarding the photocatalytic reduction of Cr(VI) by OB/Co, the photoreduction percentages increased by 55.4, 64.5, 73.4, 81.5, 89.2, 95.4, 98.2, and 100% for examined intervals of 30, 60, 90, 120, 150, 180, 210, and 240 min, respectively (Figure 6). Achieving the complete removal of Cr metal by its photoreduction into Cr(III) was attained after 240 min considering the adsorption equilibrium stage as the starting

https://dx.doi.org/10.1021/acsomega.9b03411
ACS Omega 2020, 5, 2766−2778

Table 3. Comparison between OB/Co and the Other Adsorbents Reported in the Literature Considering Their Maximum Adsorption Capacities

Cr(VI) metal			MG synthetic dye		
adsorbents	q_{max} (mg/g)	references	adsorbents	q_{max} (mg/g)	references
diatomite/magnetite	69.16	49	diatomite	23.64	62
kaolinite crusted by iron oxide	76.62	48	bentonite	7.7	63
diatomite/MCM-41	70.87	50	xerogel activated diatom	4.2	64
MnO_2 nanowire/diatomite	197.6	51	Fe-Fe_2O_3@PDA	61.22	65
carbonaceous adsorbents	56.5	52	ZnO-NRs-AC	59.17	66
FeOOH/AlOOH/MWCNTs	60.6	53	organoclay	40.4	67
diatomite	24.9	54	aerobic granules	56.8	68
MWCNTs/Fe_3O_4	76.92	55	modified carbon nanotubes	172	69
cyclodextrin/chitosan/biochars	206	56	activated carbon/zinc oxide	322.5	70
Fe_3O_4@NiO microspheres	184.2	17	carboxylate MWCNTs	11.95	44
zinc−biochar	102.6	57	cellulose nanofibril aerogels	212.7	71
oxidized SWCNTs	44.64	58	limonia acidissima	35.48	72
polyaniline	59.17	6	NiO nanoflakes	142	73
Ca-Al LDH	104.8	59	halloysite nanotubes	99.6	74
polypyrrole/Fe_3O_4 composite	243.9	60	coconut coir activated carbon	27.44	75
modified magnetic chitosan	51.8	61	Au-NP-AC	172	76
serpentine	76.33	35	iron humate	19.2	77
OB/Co composite (theoretical (Langmuir))	343.6	this study	OB/Co composite (theoretical (Langmuir))	194.5	this study
OB/Co composite (theoretical (D−R model))	226.5	this study	OB/Co composite (theoretical (D−R model))	144.6	this study
OB/Co composite (exp)	232	this study	OB/Co composite (exp)	141	this study

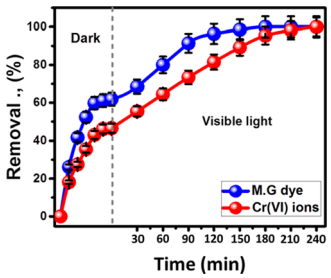

Figure 6. Photocatalytic properties of OB/Co in visible light degradation of MG.D as well as Cr metal Cr(VI).

time. The previous results give the synthetic composite (OB/Co) high technical and commercial value as products of different removal mechanism either its high adsorption properties or its effective photocatalytic properties.

2.4. Reusability Studies. Reusing the composites in a series of tests of selected adsorption and photocatalytic decontamination of MG.D and Cr metal to inspect their stability values, their reusability was assessed for five runs (Figure 7). The synthetic composite demonstrated a high stability value, which signifies that it is a suitable product for five decontamination cycles. For photocatalytic oxidation of MG.D, the achieved reusable removal percentages are 100, 97.3, 94.5, 89.2, and 85.4% for Run1, Run2, Run3, Run4, and Run5, respectively (Figure 7). For the recognized photocatalytic reduction for the studied Cr(VI) metal in the aqueous solution, the acquired reduction percentages are 100, 98.2, 95.7, 91.5, and 87.4%, respectively. Such results can be enhanced using higher quantities than 0.05 g of OB/Co as the catalyst dose (Figure 7).

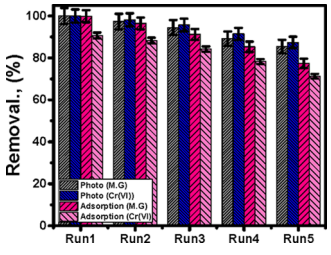

Figure 7. Reusability results of OB/Co as a photocatalyst and as an adsorbent material in the decontamination of MG.D and Cr metal.

As for reusability results for adsorption, the synthetic OB/Co composite shows high adsorption stability and the achieved percentages for the reusability test of MG.D are 99.8, 96.4, 91.2, 85.3, and 77.4%, respectively, for the five runs (Figure 7). For Cr(VI), the attained percentages are 90.7, 88.3, 84.2, 78.3, and 71.3% (Figure 7). The OB/Co composite as the adsorbent can realize higher decontamination efficiencies for more reusability tests with an increase in the removal time and the incorporated masses.

2.5. Effect of Integration and Mechanism. To examine the influence of the combination process creating a hybrid material of enhanced properties, the adsorption as well as the photocatalytic decontamination of MG.D and Cr metal was studied utilizing the composite (OB/Co) and compared with the individual components bentonite (B), organo-bentonite (OB), and cobalt oxide (Co) (Figure S4). This was accomplished after fixing the time at 240 min, the mass of the studied materials at 0.05 g, the pollutant concentration at 100 mg/L, the aqueous volume at 100 mL, the pH at 6, and the temperature at 30 °C. The adsorption percentages of MG.D by B, OB, Co, and OB/Co are 12.6, 20.5, 9.7, and 52.3%, respectively (Figure S4). This reflected enhancement in the adsorption capacity of OB/Co by 39.7, 31.8, and 42.6% as compared to the individual components B, OB, and Co, respectively. This was also observed for Cr(VI), and the uptake percentages for B, OB, Co, and OB/Co are 9.42, 16.7, 7.4, and 35.5%, respectively. i.e., the value increased by 26, 18.8, and 28% higher than the results achieved by B, OB, and Co, respectively (Figure S4).

https://dx.doi.org/10.1021/acsomega.9b03411
ACS Omega 2020, 5, 2766−2778

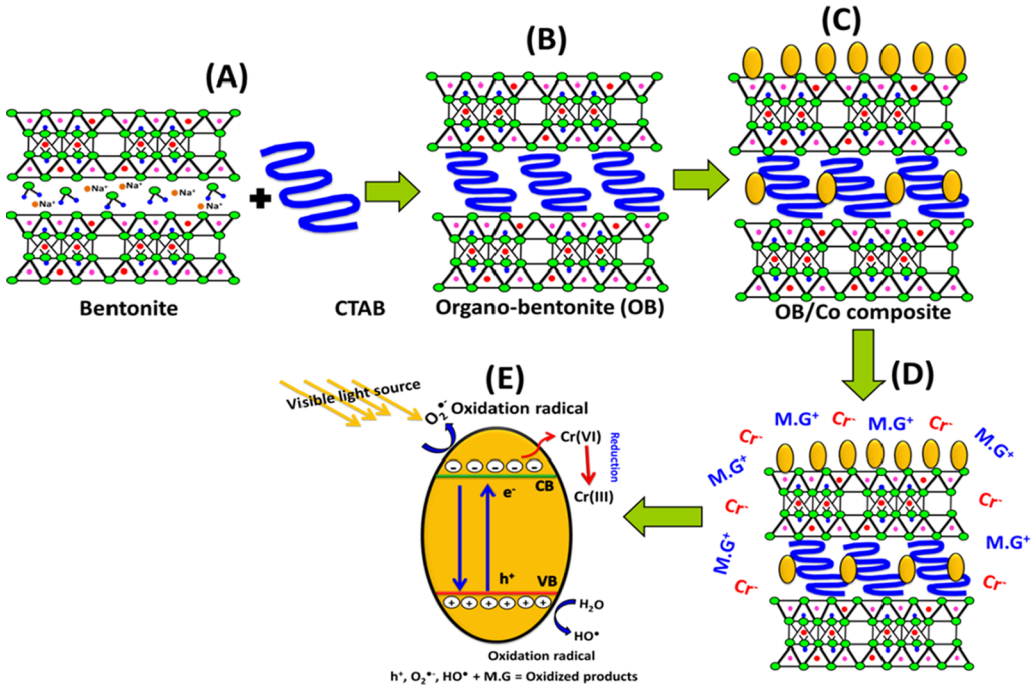

Figure 8. Schematic figures for the preparations of organically modified bentonite (OB) (A and B), the loading of green Co_3O_4 nanoparticles on the surface of OB forming the OB/Co composite (C), the enhanced adsorption of MG.D and Cr metal by the OB/Co composite (D), and the photocatalytic degradation and reduction mechanisms of MG.D and Cr metal, respectively (E).

The used pure bentonite (B) and organo-bentonite (OB) showed no photocatalytic properties and no improvement in the achieved decontamination percentages of MG.D and Cr metal. However, the pure phase of Co_3O_4 (Co) and OB/Co showed significant photocatalytic properties both in the oxidation of MG.D and the reduction of Cr metals (Figure S4). The accomplished decontamination percentages by Co and OB/Co are 38.5 and 100% for MG.D and 43.6 and 100% for the Cr metal, respectively. This reflected considerable enhancement in the photocatalytic performance of OB/Co by 61.5% for MG.D and 56.4% for the Cr(VI) metal in comparison with the green fabricated Co_3O_4 nanoparticles as a single phase.

The concluded enhancement in both the adsorption and the photocatalytic performances after supporting the Co_3O_4 nanoparticles with the organically modified bentonite might be ascribed to (a) the excellent adsorption performance of bentonite and its organic modified product, (b) the effect of the combination process, providing different types of active functional groups, (c) the distribution of Co_3O_4 homogenously over the surface of OB without agglomeration, resulting in strong impact on enhancing the total surface area, and (d) provide high exposed properties for the present active photocatalyst, which provide high chances for the interaction between the OB/Co and the incident photons.[1,78−80]

As recognized in numerous literature studies, the photocatalytic oxidation or reduction process involves three main steps in the presence of light source. First, the addressed dissolved pollutants should be adsorbed by the used catalyst followed by the absorption of the light incident photons as the second stage. After that, charge transfer occurs, forming various types of oxidizing and reducing species.[1,8] The production of the composite involves the intercalation of bentonite layers by CTAB chains, producing organically modified bentonite (OB) of high basal spacing and surface area and different types of functional groups that provide more chances for the attraction of the tested pollutants (Figure 8A,B). Afterward, the green decoration of the synthetic OB by Co_3O_4 nanoparticles results in the formation of nanograins of cobalt oxide distributed on the surface of OB without agglomeration, which can add other functional groups that contribute toward increasing the adsorption capacity (Figure 8C). The distribution of Co_3O_4 as separated grains on OB provides high chances for light interaction and to attract more MG.D molecules and Cr metals close to the active catalytic sites (Figure 8D).

The interaction between OB/Co and light photons is associated with considerable excitation of cobalt oxide electrons to the conducting band, creating electron/hole pairs and other species of oxidizing as well as reducing radicals[81] (Figure 8E). Thus, the oxidation of MG.D might be related to the electron/hole pairs or the generated hydroxyl or superoxide radicals.[1,82]

The reduction of Cr(VI) metal might be accomplished by the produced reluctant species from (a) the captured electrons during the excitation process, (b) the effect of the photogenerated $O_2^{\bullet-}$ in lowering the valence state of Cr(VI), and (c) the electron transfer effect between the OB/Co surface and the attracted Cr metals.[81,83] The illustrative equations of MG.D photocatalytic degradation and Cr(VI) photoreduction can be represented as follows (eqs 3−11)

$$\text{OB/Co} + h\nu \rightarrow \text{OB/Co}\ (e^-_{CB}, h^+_{VB}) \quad (3)$$

$$\text{OB/Co}\ (e^-) + O_2 \rightarrow \text{OB/Co} + O_2^{\bullet-} \quad (4)$$

$$(\text{OB/Co})e^- + \text{MG.D} \rightarrow (\text{OB/Co})e^- + \text{MG. D}^{+\bullet} \quad (5)$$

$$(\text{OB/Co})e^- + \text{Cr(VI)} \rightarrow (\text{OB/Co})e^- + \text{Cr(III)} \quad (6)$$

$$\text{MG. D}^{+\bullet} + O_2^{\bullet-} \rightarrow \text{degraded products} \quad (7)$$

https://dx.doi.org/10.1021/acsomega.9b03411
ACS Omega 2020, 5, 2766−2778

$$Cr(VI) + O_2^{\bullet -} \rightarrow Cr(III) + O_2 \quad (8)$$

$$OB/Co\ (h^+) + H_2O \rightarrow OB/Co + H^+ + OH^{\bullet} \quad (9)$$

$$OB/Co\ (h^+) + MG.\ D^{+\bullet} \rightarrow \text{degraded product} \quad (10)$$

$$MG.\ D^{+\bullet} + OH^{\bullet} \rightarrow \text{degraded products} \quad (11)$$

3. CONCLUSIONS

Organo-bentonite/Co_3O_4 (OB/Co) nanoparticles, a green nanocomposite, achieved experimental q_{max} of about 223 mg/g and Langmuir theoretical q_{max} of about 343.6 mg/g for MG.D; while the experimental q_{max} and Langmuir theoretical q_{max} values for Cr(VI) are 139 and 194.5 mg/g, respectively. The adsorption results of both contaminants are described excellently by the pseudo-first-order kinetic model and the Langmuir isotherm model. This reflected their favorable and homogeneous uptake in a monolayer form by physisorption mechanisms with 0.6 kJ/mol (MG.D) and 0.5 kJ/mol (Cr(VI)) adsorption energies and with D−R theoretical q_{max} values of 226.5 and 144.6 mg/g, respectively. The thermodynamic parameters revealed physical, spontaneous, and exothermic uptake of MG.D and Cr(VI) metal. Also, the composite showed high photocatalytic performance under visible light, which appeared in complete oxidation and reduction of 100 mg/L of MG.D and Cr metal after about 180 and 240 min, respectively.

4. EXPERIMENTAL SECTION

4.1. Materials. The used natural bentonite samples were raw samples collected from local bentonite quarry, Northern Western Desert, Egypt. Cetyltrimethylammonium bromide (Sigma Aldrich (CTAB, 99%)) was incorporated during the organic modification of the bentonite sample. Cobalt nitrate hexahydrate of analytical grade and of >98% purity (Sigma Aldrich, Egypt) was used in the production of Co_3O_4 oxide. NaOH scales and HCl dilute solution were supplied by El-Nasr Chemical Company and were used as pH modifiers.

4.2. Synthesis of Organo-bentonite. The fabrication of organically modified bentonite was accomplished by direct intercalation of bentonite layers by CTAB chains. The studied bentonite powder (2 g) was ground and dispersed homogeneously within 100 mL of distilled water and stirred at 500 rpm for 2 h. After that, 1 g of the CTAB surfactant was dissolved within 50 mL of distilled water, and then, the resulted mixture was stirred for another 30 min to confirm its complete dissolution. Then, the prepared surfactant solution was mixed with the bentonite suspension and the mixture was stirred for 24 h at 70 °C. Finally, the solid fractions were separated using a centrifuge, washed extensively five times with distilled water, and dried in an electric oven at 80 °C for about 12 h.

4.3. Green Fabrication of Organo-bentonite/Cobalt Oxide (OB/Co) Composite. First, the reducing reagent was extracted from green tea by boiling 5 g of it in 100 mL of distilled water for 5 min and 100 mL of the resulting extract was kept to be used in the formation of cobalt oxide. Furthermore, 3 g of the prepared organo-bentonite was dispersed in 50 mL of distilled water under ultrasonic irradiation for 60 min. Then, 50 mL of an aqueous solution containing about 2.5 g of dissolved cobalt nitrate hexahydrate was mixed with the organo-bentonite suspension under stirring for another 60 min at 500 rpm. After that, the green tea extract was mixed with this under stirring and the mixture was left at room temperature for 48 h to confirm the successful loading of organo-bentonite by nano cobalt oxide. Finally, the solid fractions were separated using the centrifuge, washed, and dried for 10 h at 60 °C.

4.4. Characterization Techniques. The crystalline phases were identified considering the X-ray diffraction patterns that were obtained using an X-ray diffractometer of PANalytical (Empyrean) type. The surface morphology and the internal features were investigated based on SEM and HRTEM images obtained utilizing a scanning electron microscope (Gemini, Zeiss-Ultra 55) and a transmission electron microscope (JEOL-JEM2100), respectively. The change in the functional groups was followed based on the obtained absorption bands of FT-IR spectra using an FT-IR Raman spectrometer (Vertex 70). The optical properties of the OB/CO composite were examined within a light range from 200 nm to about 800 nm by a Shimadzu-M160 PC UV−vis spectrophotometer. The textural properties including the surface area and pore size distribution were estimated using the Brunauer−Emmett−Teller method and Barrett−Joyner−Halenda method, respectively.

4.5. Adsorption System. The adsorption properties of the OB/Co composite for MG.D and Cr(VI) metals were evaluated using a UV−vis spectrophotometer and inductively coupled plasma, respectively. The experiment was repeated three times, and the obtained results are the average values with standard deviations lower than 5.4% for MG.D and 3.8% for Cr(VI) metals.

4.5.1. Effect of pH. Addressing the influence of adsorption pH on the affinity of OB/Co for MG.D and Cr metals was accomplished at various pH values from 2 to 8. The other affecting factors were fixed at 0.05 g of OB/Co mass, 100 mL of polluted solution volume, 100 mg/L as the contaminant concentration, 30 °C temperature, and 240 min as the studied time interval.

4.5.2. Effect of Time and Kinetic Studies. The influence of time and the related kinetic behavior were inspected with a time range from about 5 min to about 720 min after fixing the controlling factors at 0.05 g of OB/Co mass, 100 mL of polluted solution volume, 100 mg/L as contaminant concentration, 30 °C temperature, and pH 6. The kinetic properties of OB/Co adsorption systems were evaluated considering the assumptions of three theoretical models (pseudo-first-order kinetic model, Lagergren pseudo-second-order model, Elovich model, and intraparticle diffusion model) by linear regression fitting with their representative equations eqs 12−15, respectively.

$$\ln(q_e - q_t) = \ln q_e - k_1 t \quad (12)$$

$$\frac{t}{q_t} = \frac{1}{K_2 q_e^2} + \frac{t}{q_e} \quad (13)$$

$$q_t = \frac{1}{\beta}\ln(\alpha\beta) + \frac{1}{\beta}\ln(t) \quad (14)$$

$$q_t = K_p t^{1/2} + C \quad (15)$$

4.5.3. Effect of OB/Co Mass. The possible enhancement in the removal percentages of certain concentrations of the studied contaminants with incorporation of higher quantities of OB/Co was investigated within a range from 0.05 to 0.3 g

https://dx.doi.org/10.1021/acsomega.9b03411
ACS Omega 2020, 5, 2766−2778

after fixing the controlling factors at 100 mL of polluted solution volume, 100 mg/L as contaminant concentration, 240 min as time, 30 °C temperature, and pH 6.

4.5.4. Equilibrium Studies. The effect of increasing the initial concentrations of the studied contaminants on the uptake capacity as well as the equilibrium behaviors was addressed for different concentrations within the experimental range from 50 to 300 mg/L. The additional affecting factors were fixed at 0.05 g as OB/Co mass, 100 mL of the polluted solution as the treated volume, 100 mg/L as the contaminant concentration, 30 °C temperature, and 480 as the studied time interval. The equilibrium behaviors were evaluated based on the results of the linear regression fitting with different theoretical isotherm models including Langmuir, Freundlich, and Dubinin−Radushkevich models, and their representative equations are eqs 16−18, respectively.[2]

$$\frac{C_e}{q_e} = \frac{1}{bq_{max}} + \frac{C_e}{q_{max}} \quad (16)$$

$$\log q_e = (1/n) \log C_e + \log K_F \quad (17)$$

$$\ln(q_e) = \ln(q_m) - \beta\varepsilon^2 \quad (18)$$

4.5.5. Thermodynamic Properties. The thermodynamic properties of the OB/Co-based adsorption system for MG.D and Cr metal were studied considering the reaction temperature from 298 to 333 K. The other affecting factors were fixed at 0.05 g as OB/Co mass, 100 mL of the polluted solution volume, 100 mg/L as contaminant concentration, and 720 min as the studied time interval.

4.6. Photocatalytic Studies. The photocatalytic properties of OB/Co in visible light decontamination of MG.D and Cr(VI) metals at 100 mg/L concentration were studied using a metal halide lamp (400 W) with 490 nm average wavelength. All tests were conducted after attending the adsorption/desorption equilibrium of MG.D and Cr(VI) within time intervals from 30 to 240 min using 0.05 g of OB/Co as the photocatalyst mass at pH 6 and 30 °C as temperature.

4.7. Reusability Study. The suitability of using OB/Co for several runs of MG.D and Cr(VI) removal either as an adsorbent or as a photocatalyst is a vital factor for its realistic use on a commercial scale. OB/Co (0.05 and 0.3 g) for the adsorption and photocatalytic reusability tests, respectively, was mixed with 100 mL of contaminated solutions (100 mg/L) for 240 min at pH 6 and room temperature. By the end of each cycle, the solid fractions were isolated, washed by distilled water, and dried to be used in the other cycles.

■ ASSOCIATED CONTENT

Supporting Information

The Supporting Information is available free of charge at https://pubs.acs.org/doi/10.1021/acsomega.9b03411.

EDX analysis of the organo-bentonite/Co_3O_4 composite (Figure S1); FT-IR spectra of raw bentonite, organo-bentonite, and the composite (Figure S2); the fitting of the adsorption results with the Elovich model (Figure S3); and the influence of the combination process on the adsorption as well as the photocatalytic decontamination of the Cr metal and malachite green synthetic dye (Figure S4) (PDF)

■ AUTHOR INFORMATION

Corresponding Author

Mostafa R. Abukhadra − *Materials Technologies and Their Applications Lab, Geology Department, Faculty of Science and Geology Department, Faculty of Science, Beni-Suef University, Beni Suef City 62521, Egypt*; orcid.org/0000-0001-5404-7996; Email: Abukhadra89@Science.bsu.edu.eg

Authors

Mohamed Abdel Salam − *Chemistry Department, Faculty of Science, King Abdulaziz University, Jeddah 21589, Kingdom of Saudi Arabia*

Alyaa Adlii − *Materials Technologies and Their Applications Lab, Geology Department, Faculty of Science and Department of Chemistry, Faculty of Education, Beni-Suef University, Beni Suef City 62521, Egypt*

Complete contact information is available at: https://pubs.acs.org/10.1021/acsomega.9b03411

Author Contributions

This article was written through the contributions of all authors. All authors have given approval to the final version of the manuscript.

Notes

The authors declare no competing financial interest.

Further studies will be conducted to evaluate the main adsorption mechanisms of the assessed composite for different types of pollutants in the presence of coexisting ions.

■ ACKNOWLEDGMENTS

This work was supported by the Deanship of Scientific Research (DSR), King Abdulaziz University, Jeddah, under grant No. (DF-109-130-1441). The authors, therefore, gratefully acknowledge DSR technical and financial support.

■ ABBREVIATIONS

B	bentonite
OB	organo-bentonite
Co	Co_3O_4
OB/Co	organo-bentonite/Co_3O_4 composite
CTAB	cetyltrimethylammonium bromide
MG.D	synthetic Malachite green basic dye
Cr(VI) metal	hexavalent chromium metal
t	time intervals
q_t	the uptake capacity at certain time interval in mg/g
K_2	the rate constant of the Lagergren kinetic model in g/mg min
α	the initial uptake rate in mg/min
β	the surface saturation value in g/mg
C_e	the remaining concentrations of the dye and the metal in mg/L
q_e	the equilibration adsorption capacity in mg/g
q_{max}	the theoretically estimated maximum uptake capacity in mg/g
b	the constant of Langmuir isotherm in L/mg
K_F	the constant of the studied Freundlich model, which is related to the adsorption capacities
n	the constant of the studied Freundlich model, which is related to the uptake intensities
$\Delta G°$	the Gibbs free energy of the adsorption system in kJ/mol

https://dx.doi.org/10.1021/acsomega.9b03411
ACS Omega 2020, 5, 2766−2778

ΔH°	the standard enthalpy of the adsorption reaction in kJ/mol
ΔS°	the entropy of the adsorption reaction in kJ/mol
R	the gas constant
T	the adsorption absolute temperature
K_c	the Langmuir constant
B	the constant of D−R model in mol^2/kJ^2
ε	the Polanyil potential of the D−R model in kJ^2/mol^2
q_m	the D−R theoretical adsorption capacities in mg/g

REFERENCES

(1) Abukhadra, M. R.; Shaban, M.; Sayed, F.; Saad, I. Efficient photocatalytic removal of safarnin-O dye pollutants from water under sunlight using synthetic bentonite/polyaniline@Ni_2O_3 photocatalyst of enhanced properties. *Environ. Sci. Pollut. Res.* **2018**, *25*, 33264−33276.

(2) Abukhadra, M. R.; Bakry, B. M.; M.R. Adlii, A.; Yakout, S. M.; El-Zaidy, M. A. Facile conversion of kaolinite into clay nanotubes (KNTs) of enhanced adsorption properties for toxic heavy metals (Zn^{2+}, Cd^{2+}, Pb^{2+}, and Cr^{6+}) from water. *J. Hazard. Mater.* **2019**, *374*, 296−308.

(3) Wu, Y.; Li, X.; Yang, Q.; Wang, D.; Xu, Q. G.; Yao, F.; Chen, F.; Tao, Z.; Huan, X. Hydrated lanthanum oxide-modified diatomite as highly efficient adsorbent for low-concentration phosphate removal from secondary effluents. *J. Environ. Manage.* **2019**, *231*, 370−379.

(4) Mohamed, A.; Ghobara, M. M.; Abdelmaksoud, M. K.; Mohamed, G. G. A novel and highly efficient photocatalytic degradation of malachite green dye via surface modified polyacrylonitrile nanofibers/biogenic silica composite nanofibers. *Sep. Purif. Technol.* **2019**, *210*, 935−942.

(5) Shi, Z.; Xu, C.; Guan, H.; Li, L.; Fan, L.; Wang, Y.; Liu, L.; Meng, Q.; Zhang, R. Magnetic metal organic frameworks (MOFs) composite for removal of lead and malachite green in wastewater. *Colloids Surf., A* **2018**, *539*, 382−390.

(6) Shaban, M.; Abukhadra, M. R.; Rabia, M.; Elkader, Y. A.; El-Halim, M. R. A. Investigation the adsorption properties of graphene oxide and polyaniline nano/micro structures for efficient removal of toxic Cr(VI) contaminants from aqueous solutions; kinetic and equilibrium studies. *Rend. Lincei* **2018**, *29*, 141−154.

(7) Khan, T. A.; Nazir, M.; Ali, I.; Kumar, A. Removal of Chromium (VI) from aqueous solution using guar gum−nano zinc oxide biocomposite adsorbent. *Arabian J. Chem.* **2017**, *10*, S2388−S2398.

(8) Mohamed, F.; Abukhadra, M. R.; Shaban, M. Removal of safranin dye from water using polypyrrole nanofiber/Zn-Fe layered double hydroxide nanocomposite (Ppy NF/Zn-Fe LDH) of enhanced adsorption and photocatalytic properties. *Sci. Total Environ.* **2018**, *640−641*, 352−363.

(9) Wu, Q.; Zhang, Z. The preparation of self-floating Sm/N co-doped TiO_2/diatomite hybrid pellet with enhanced visible-light-responsive photoactivity and reusability. *Adv. Powder Technol.* **2019**, *30*, 415−422.

(10) Khan, T. A.; Rahman, R.; Ali, I.; Khan, E. A.; Mukhlif, A. A. Removal of malachite green from aqueous solution using waste pea shells as low-cost adsorbent−adsorption isotherms and dynamics. *Toxicol. Environ. Chem.* **2014**, *96*, 569−578.

(11) Dhas, C. R.; Venkatesha, R.; Jothivenkatachalamb, K.; Nithyab, A.; Benjaminc, B. S.; Rajc, A. M. E.; Jeyadheepand, K.; Sanjeevirajae, C. Visible light driven photocatalytic degradation of Rhodamine B and Direct Red using cobalt oxide nanoparticles. *Ceram. Int.* **2015**, *41*, 9301−9313.

(12) Xu, Y.; Wang, L.; Cao, P.; Cai, C.; Fu, Y.; Ma, X. Mesoporous composite nickel cobalt oxide/graphene oxide synthesized via a template-assistant co-precipitation route as electrode material for supercapacitors. *J. Power Sources* **2016**, *306*, 742−752.

(13) Khan, M. N.; Bashir, O.; Khan, T. A.; Al-Thabaiti, S. A.; Khan, Z. Catalytic Activity of Cobalt Nanoparticles for Dye and 4-Nitro Phenol Degradation: A Kinetic and Mechanistic Study. *Int. J. Chem. Kinet.* **2017**, *49*, 438−454.

(14) Soliemanzadeh, A.; Fekri, M. Synthesis of clay-supported nanoscale zero-valent iron using green tea extract for the removal of phosphorus from aqueous solutions. *Chin. J. Chem. Eng.* **2017**, *25*, 924−930.

(15) Khan, M. N.; Bashir, O.; Khan, T. A.; Al-Thabaiti, S. A.; Khan, Z. CTAB capped synthesis of bio-conjugated silver nanoparticles and their enhanced catalytic activities. *J. Mol. Liq.* **2018**, *258*, 133−141.

(16) Zhu, P.; Chen, Y.; Duan, M.; Liu, M.; Zou, P. Structure and properties of Ag_3PO_4/diatomite photocatalysts for the degradation of organic dyes under visible light irradiation. *Powder Technol.* **2018**, *336*, 230−239.

(17) Zhang, S.; Li, J.; Wen, T.; Xu, J.; Wang, X. Magnetic Fe_3O_4@NiO hierarchical structures: preparation and their excellent As (V) and Cr(VI) removal capabilities. *RSC Adv.* **2013**, *3*, 2754−2764.

(18) Shaban, M.; Abukhadra, M. R.; Shahien, M. G.; Ibrahim, S. S. Novel bentonite/zeolite-NaP composite efficiently removes methylene blue and Congo red dyes. *Environ. Chem. Lett.* **2018**, *16*, 275−280.

(19) Dardir, F. M.; Mohamed, A. S.; Abukhadra, M. R.; Ahmed, E. A.; Soliman, M. F. Cosmetic and pharmaceutical qualifications of Egyptian bentonite and its suitability as drug carrier for Praziquantel drug. *Eur. J. Pharm. Sci.* **2018**, *115*, 320−329.

(20) Li, N.; Yang, B.; Xu, L.; Xu, G.; Sun, W.; Yu, S. Simple synthesis of Cu_2O/Na-bentonite composites and their excellent photocatalytic properties in treating methyl orange solution. *Ceram. Int.* **2016**, *42*, 5979−5984.

(21) Kassir, M.; Roques-Carmes, T.; Pelletier, M.; Bihannic, I.; Alem, H.; Hamieh, T.; Toufaily, J.; Villiéras, F. Adsorption and photocatalysis activity of TiO_2/bentonite composites. *Desalin. Water Treat.* **2017**, *98*, 196−215.

(22) Cao, X.; Luo, S.; Liu, C.; Chen, J. Synthesis of Bentonite-Supported Fe_2O_3-Doped TiO_2 superstructures for highly promoted photocatalytic activity and recyclability. *Adv. Powder Technol.* **2017**, *28*, 993−999.

(23) Mishra, A.; Mehta, A.; Sharma, M.; Basu, S. Impact of Ag Nanoparticles on Photomineralization of Chlorobenzene by TiO_2/Bentonite Nanocomposite. *J. Environ. Chem. Eng.* **2017**, *5*, 644−651.

(24) Patil, S. P.; Bethi, B.; Sonawane, G. H.; Shrivastava, V. S.; Sonawane, S. Efficient adsorption and photocatalytic degradation of Rhodamine B3 dye over Bi_2O_3-bentonite nanocomposites: A kinetic study. *Ind. Eng. Chem.* **2016**, *34*, 356−363.

(25) de Mattos Amadio, T. M.; Hotza, D.; Neto, J. B. R.; Blosi, M.; Costa, A. L.; Dondi, M. Bentonites functionalized by impregnation with TiO_2, Ag, Pd and Au Nanoparticles. *Appl. Clay Sci.* **2017**, *146*, 1−6.

(26) Abukhadra, M. R.; Refay, N. M.; El-Sherbeeny, A. M.; Mostafa, A. M.; Elmeligy, M. A. Facile synthesis of bentonite/biopolymer composites as low-cost carriers for 5-fluorouracil drug; equilibrium studies and pharmacokinetic behavior. *Int. J. Biol. Macromol.* **2019**, *141*, 721−731.

(27) Seliem, M. K.; Komarneni, S.; Cho, Y.; Lim, T.; Shahien, M. G.; Khalil, A. A.; Abd El-Gaid, I. M. Organosilicas and organo-clay minerals as sorbents for toluene. *Appl. Clay Sci.* **2011**, *52*, 184−189.

(28) Shettigar, R. R.; Misra, N. M.; Patel, K.; Petrol, J. Cationic surfactant (CTAB) a multipurpose additive in polymer-based drilling fluids. *J. Pet. Explor. Prod. Technol.* **2018**, *8*, 597−606.

(29) Saha, N. R.; Sarkar, G.; Roy, I.; Bhattacharyya, A.; Rana, D.; Dhanarajan, G.; Banerjee, R.; Sen, R.; Mishrad, R.; Chattopadhyay, D. Nanocomposite films based on cellulose acetate/polyethylene glycol/modified montmorillonite as nontoxic active packaging material. *RSC Adv.* **2016**, *6*, 92569−92578.

(30) Verma, A. K.; Dash, R. R.; Bhunia, P. A review on chemical coagulation flocculation technologies for removal of colour from textile wastewaters. *J. Environ. Manage.* **2012**, *93*, 154−168.

https://dx.doi.org/10.1021/acsomega.9b03411
ACS Omega 2020, 5, 2766−2778

(31) Zeng, J.; Zhe, Z.; Zhihui, D.; Panfeng, R.; Yuan, L.; Xiao, L. Fabrication and characterization of an ion-imprinted membrane via blending poly(methyl methacrylate-co-2-hydroxyethyl methacrylate) with polyvinylidenefluoride for selective adsorption of Ru(III). *React. Funct. Polym.* **2017**, *115*, 1−9.
(32) Diallo, A.; Beye, A. C.; Doyle, T. B.; Park, E.; Maaza, M. Green synthesis of Co_3O_4 nanoparticles via Aspalathus linearis: Physical properties. *Green Chem. Lett. Rev.* **2015**, *8*, 30−36.
(33) Fu, H.; Yang, Y.; Zhu, R.; Liu, J.; Usman, M.; Chen, Q.; He, H. Superior adsorption of phosphate by ferrihydrite-coated and lanthanum-decorated magnetite. *J. Colloid Interface Sci.* **2018**, *530*, 704−713.
(34) Pepper, R. A.; Couperthwaite, S. J.; Millar, G. J. Re-use of waste red mud: Production of a functional iron oxide adsorbent for removal of phosphorous. *J. Water Process Eng.* **2018**, *25*, 138−148.
(35) Shaban, M.; Abukhadra, M. R.; Parwaz, A. A.; Jabili, B. M. Removal of Congo red, methylene blue and Cr(VI) ions from water using natural serpentine. *J. Taiwan Inst. Chem. Eng.* **2018**, *82*, 102−116.
(36) Alshameri, A.; He, H.; Zhu, J.; Xi, Y.; Zhu, R.; Ma, L.; Tao, Q. Adsorption of ammonium by different natural clay minerals: characterization, kinetics and adsorption isotherms. *Appl. Clay Sci.* **2018**, *159*, 83−93.
(37) Amghouz, Z.; Ancín-Azpilicueta, C.; Burusco, K. K.; García, J. R.; Khainakov, S. A.; Luquin, A.; Nieto, R.; Garrido, J. J. Biogenic amines in wine: individual and competitive adsorption on a modified zirconium phosphate. *Microporous Mesoporous Mater.* **2014**, *197*, 130−139.
(38) Giles, C. H.; MacEwan, T. H.; Nakhwa, S. N.; Smith, D. Studies in adsorption. Part XI. A system of classification of solution adsorption isotherms, and its use in diagnosis of adsorption mechanisms and in measurement of specific surface areas of solids. *J. Chem. Soc.* **1960**, 3973−3993.
(39) Tu, Y.; Feng, P.; Ren, Y.; Cao, Z.; Wang, R.; Xu, Z. Adsorption of ammonia nitrogen on lignite and its influence on coal water slurry preparation. *Fuel* **2019**, *238*, 34−43.
(40) Huang, Y.; Li, S.; Chen, J.; Zhang, X.; Chen, Y. Adsorption of Pb(II) on mesoporous activated carbons fabricated from water hyacinth using H_3PO_4 activation: Adsorption capacity, kinetic and isotherm studies. *Appl. Surf. Sci.* **2014**, *293*, 160−168.
(41) Abukhadra, M. R.; Mostafa, M. Effective decontamination of phosphate and ammonium utilizing novel muscovite/phillipsite composite; equilibrium investigation and realistic application. *Sci. Total Environ.* **2019**, *667*, 101−111.
(42) Raghu, M. S.; Yogesh Kumar, K.; Prashanth, M. K.; Prasanna, B. P.; Vinuth, R.; Pradeep Kumar, C. B. Adsorption and antimicrobial studies of chemically bonded magnetic graphene oxide-Fe_3O_4 nanocomposite for water purification. *J. Water Process Eng.* **2017**, *17*, 22−31.
(43) Rong, X.; Qiu, F.; Qin, J.; Zhao, H.; Yan, J.; Yang, D. A facile hydrothermal synthesis, adsorption kinetics and isotherms to Congo Red azo-dye from aqueous solution of NiO/graphene nanosheets adsorbent. *J. Ind. Eng. Chem.* **2015**, *26*, 354−363.
(44) Rajabi, M.; Mirzab, B.; Mahanpoor, K.; Najafi, F.; Moradif, O.; Sadegh, H.; Shahryari-ghoshekandi, R.; Asif, M.; Tyagi, I.; Agarwal, S.; Gupta, V. K.; et al. Adsorption of malachite green from aqueous solution by carboxylate group functionalized multi-walled carbon nanotubes: Determination of equilibrium and kinetics parameters. *J. Ind. Eng. Chem.* **2016**, *34*, 130−138.
(45) El Bouraie, M.; Masoud, A. A. Adsorption of phosphate ions from aqueous solution by modified bentonite with magnesium hydroxide Mg (OH) $_2$. *Appl. Clay Sci.* **2017**, *140*, 157−164.
(46) Lin, H.; Wu, X.; Zhu, J. Reduction of chromium (VI) by pyrite in dilute aqueous solutions. *S Sep. Sci. Technol.* **2016**, *51*, 202−213.
(47) Mohagheghian, A.; Pourmohseni, M.; Vahidi-Kolur, R.; Yang, J. K.; Shirzad-Siboni, M. Preparation and characterization of kaolin coated with Fe_3O_4 nanoparticles for the removal of hexavalent chromium: Kinetic, equilibrium and thermodynamic studies. *Desalin. Water Treat.* **2017**, *90*, 262−272.
(48) Yuan, W.; Yuan, P.; Liu, D.; Yu, W.; Laipan, M.; Deng, L.; Chen, F. In situ hydrothermal synthesis of a novel hierarchically porous TS-1/modified-diatomite composite for methylene blue (MB) removal by the synergistic effect of adsorption and photocatalysis. *J. Colloid Interface Sci.* **2016**, *462*, 191−199.
(49) Selim, A. Q.; Mohamed, E. A.; Mobarak, M.; Zayed, A. M.; Seliem, M. K.; Komarneni, S. Cr(VI) uptake by a composite of processed diatomite with MCM-41: Isotherm, kinetic and thermodynamic studies. *Microporous Mesoporous Mater.* **2018**, *260*, 84−92.
(50) Du, Y.; Wang, L.; Wang, J.; Zheng, G.; Wu, J.; Dai, H. Flower-, wire-, and sheet-like MnO_2-deposited diatomites: Highly efficient absorbents for the removal of Cr(VI). *J. Environ. Sci.* **2015**, *29*, 71−81.
(51) Jain, M.; Garg, V. K.; Kadirvelu, K. Adsorption of hexavalent chromium from aqueous medium onto carbonaceous adsorbents prepared from waste biomass. *J. Environ. Manage.* **2010**, *91*, 949−957.
(52) Barakat, M. A.; Al-Ansari, A. M.; Kumar, R. Synthesis and characterization of Fe−Al binary oxyhydroxides/MWCNTs nanocomposite for the removal of Cr(VI) from aqueous solution. *J. Taiwan Inst. Chem. Eng.* **2016**, *63*, 303−311.
(53) Du, Y.; Wang, X.; Wu, J.; Qi, C.; Li, Y. Adsorption and photoreduction of Cr(VI) via diatomite modified by Nb_2O_5 nanorods. *Particuology* **2018**, *40*, 123−130.
(54) Ghasemi, R.; Sayahi, T.; Tourani, S. Modified Magnetite Nanoparticles for Hexavalent Chromium Removal from Water. *J. Dispersion Sci. Technol.* **2016**, *37*, 1303−1314.
(55) Huang, X.; Liu, Y.; Liu, S.; Tan, X.; Ding, Y.; Zeng, G.; Zhou, Y.; Zhang, M.; Wangab, S.; Zheng, B. Effective removal of Cr(VI) using b-cyclodextrin− chitosan modified biochars with adsorption/reduction bifuctional roles. *RSC Adv.* **2016**, *6*, 94−104.
(56) Jiang, T.-Y.; Jiang, J.; Xu, R.-K.; Li, Z. Adsorption of Pb(II) on variable charge soils amended with rice-straw derived biochar. *Chemosphere* **2012**, *89*, 249−256.
(57) Najafpoor, A. A.; Soleimani, G.; Ehrampoush, M. H.; Ghaneian, M. T.; Salmani, E. R.; Takabi, M. D. Study on the adsorption isotherms of chromium (VI) by means of carbon nano tubes from aqueous solutions. *Environ. Health Eng. Manage. J.* **2014**, *1*, 1−5.
(58) Li, Y. L.; Wang, J.; Li, Z. S.; Liu, Q.; Liu, J. Y.; Liu, L. H.; Zhang, X. F.; Yu, J. Ultrasound assisted synthesis of Ca−Al hydrotalcite for U(VI) and Cr(VI) adsorption. *Chem. Eng. Water Res. J.* **2013**, *218*, 295−302.
(59) Bhaumik, M.; Maity, A.; Srinivasu, V. V.; Onyango, M. S. Enhanced removal of Cr(VI) from aqueous solution using polypyrrole/Fe_3O_4 magnetic nanocomposite. *J. Hazard. Mater.* **2011**, *190*, 381−390.
(60) Hu, X. J.; Wang, J. S.; Liu, Y. G.; Li, X.; Zeng, G. M.; Bao, Z. L.; Zeng, X. X.; Chen, A. W.; Long, F. Adsorption of chromium (VI) by ethylenediamine-modified cross-linked magnetic chitosan resin: isotherms, kinetics and thermodynamics. *J. Hazard. Mater.* **2011**, *185*, 306−314.
(61) Tian, L.; Zhang, J.; Shi, H.; Li, N.; Ping, Q. Adsorption of Malachite Green by Diatomite: Equilibrium Isotherms and Kinetics Studies. *J. Dispersion Sci. Technol.* **2016**, *37*, 1059−1066.
(62) Tahir, S. S.; Rauf, N. Removal of Cationic Dye from Aqueous Solutions by Adsorption onto Bentonite Clay. *Chemosphere* **2006**, *63*, No. 1842.
(63) Sriram, G.; Uthappa, U. T.; Kigga, M.; Jung, H. Y.; Altalhi, T.; Brahmkhatri, V.; Kurkuri, M. D. Xerogel activated diatom as an effective hybrid adsorbent for the efficient removal of malachite green. *New J. Chem.* **2019**, *43*, 3810−3820.
(64) Wang, K.; Fu, J.; Wang, S.; Gao, M.; Zhu, J.; Wang, Z.; Xu, Q. Polydopamine-coated magnetic nanochains as efficient dye adsorbent with good recyclability and magnetic separability. *J. Colloid Interface Sci.* **2018**, *516*, 263−273.
(65) Azad, F. N.; Ghaedi, M.; Dashtian, K.; Hajati, S.; Goudarzi, A.; Jamshidi, M. Enhanced simultaneous removal of malachite green and safranin O by ZnO nanorod-loaded activated carbon: modeling, optimization and adsorption isotherms. *New J. Chem.* **2015**, *39*, 7998−8005.

https://dx.doi.org/10.1021/acsomega.9b03411
ACS Omega 2020, 5, 2766−2778

(66) Arellano-Cárdenas, S.; López-Cortez, S.; Cornejo-Mazón, M.; Mares-Gutiérrez, J. C. Study of malachite green adsorption by organically modified clay using a batch method. *Appl. Surf. Sci.* **2013**, *280*, 74−78.
(67) Sun, X. F.; Wang, S. G.; Liu, X. W.; Gong, W. X.; Bao, N.; Gao, B. Y.; Zhang, H. Y. Biosorption of Malachite Green from aqueous solutions onto aerobic granules: kinetic and equilibrium studies. *Bioresour. Technol.* **2008**, *99*, 3475−3483.
(68) Awadallah-f, A. Adsorptive removal of malachite green chloride and reactive red-198 from aqueous solutions by using multiwall carbon nanotubes-graft-poly (2-acrylamido-2-methyl-1-propanesulfonic acid). *J. Polym. Environ.* **2017**, *25*, 258−276.
(69) Ghaedi, M.; Ansari, A.; Habibi, M. H.; Asghari, A. R. Removal of malachite green from aqueous solution by zinc oxide nanoparticle loaded on activated carbon: Kinetics and isotherm study. *J. Ind. Eng. Chem.* **2014**, *20*, 17−28.
(70) Jiang, F.; Dinh, D. M.; Hsieh, Y. L. Adsorption and desorption of cationic malachite green dye on cellulose nanofibril aerogels. *Carbohydr. Polym.* **2017**, *173*, 286−294.
(71) Sartape, A. S.; Mandhare, A. M.; Jadhav, V. V.; Raut, P. D.; Anuse, M. A.; Kolekar, S. S. Removal of malachite green dye from aqueous solution with adsorption technique using Limonia acidissima(wood apple) shell as low cost adsorbent. *Arabian J. Chem.* **2017**, *10*, S3229−S3238.
(72) Wei, A.; Liu, B.; Zhao, H.; Chen, Y.; Wang, W.; Ma, Y.; Yang, H.; Liu, S. Synthesis and formation mechanism of flower like architectures assembled from ultrathin NiO nanoflakes and their adsorption to malachite green and acid red in water. *Chem. Eng. J.* **2014**, *239*, 141−148.
(73) Kiani, G.; Dostali, M.; Rostami, A. A. Adsorption studies on the removal of malachite green from aqueous solutions onto halloysite nanotubes. *Appl. Clay Sci.* **2011**, *54*, 34−39.
(74) Uma, S.; Banerjee, Y. C.; Sharma, J. Equilibrium and kinetic studies for removal of malachite green from aqueous solution by a low cost activated carbon. *Ind. Eng. Chem.* **2013**, *19*, No. 1099.
(75) Roosta, M.; Ghaedi, M.; Shokri, N.; Daneshfar, A.; Sahraei, R.; Asghari, A. Optimization of the combined ultrasonic assisted/adsorption method for the removal of malachite green by gold nanoparticles loaded on activated carbon: experimental design. *Spectrochim. Acta, Part A* **2014**, *118*, 55−65.
(76) Janoš, P. Sorption of Basic Dyes onto Iron Humate. *Environ. Sci. Technol.* **2003**, *37*, No. 5792.
(77) Li, J.; Xuejiang, W.; Jian, W.; Yuan, L.; Siqing, X.; Jianfu, Z. Simultaneous recovery of microalgae, ammonium and phosphate from simulated wastewater by MgO modified diatomite. *Chem. Eng. J.* **2019**, *362*, 802−811.
(78) Prabhu, V. G.; Paloly, A. R.; Divya, N. G.; Bushiri, M. J. Photocatalytic and ferromagnetic properties of electrically conducting multifunctional Ni/NiO nanocomposites in amorphous carbon matrix. *Mater. Sci. Eng., B* **2018**, *228*, 132−141.
(79) Wang, L.; Liu, M.; Wang, G.; Dai, B.; Yu, F.; Zhang, J. An ultralight nitrogen-doped carbon aerogel anchored by Ni-NiO nanoparticles for enhanced microwave adsorption performance. *J. Alloys Compd.* **2019**, *776*, 43−51.
(80) Sun, Q.; Hu, X.; Zheng, S.; Zhang, J.; Sheng. Effect of calcination on structure and photocatalytic property of $NTiO_2$/g-C_3N_4@diatomite hybrid photocatalyst for improving reduction of Cr(VI). *Environ. Pollut.* **2019**, *245*, 53−62.
(81) Chouchene, B.; Ben Chaabane, T.; Balan, L.; Girot, E.; Mozet, K.; Ghouti, M.; Schneider, R. High performance Ce-doped ZnO nanorods for sunlight-driven photocatalysis. *Beilstein J. Nanotechnol.* **2016**, *7*, 1338−1349.
(82) Lin, Y. T.; Huang, C. P. Reduction of chromium (VI) by pyrite in dilute aqueous solutions. *Sep. Purif. Technol.* **2008**, *63*, 191−199.
(83) Diao, Z.-H.; Xu, X.-R.; Liu, F.-M.; Sun, Y.-X.; Zhang, Z.-W.; Sun, K.-F.; Wang, S.-Z.; Cheng, H. Photocatalytic degradation of malachite green by pyrite and its synergism with Cr(VI) reduction: Performance and reaction mechanism. *Sep. Purif. Technol.* **2015**, *154*, 168−175.

https://dx.doi.org/10.1021/acsomega.9b03411
ACS Omega 2020, 5, 2766−2778